EPJ Applied Metamaterials

Terahertz metamaterials

RESEARCH ARTICLE

OPEN ⭗ ACCESS

Singular graphene metasurfaces

Emanuele Galiffi[*], John Pendry, and Paloma Arroyo Huidobro

The Blackett Laboratory, Department of Physics, Imperial College London, Prince Consort Road, SW72AZ, London, UK

Abstract. The spatial tunability of the electron density in graphene enables the dynamic engineering of metasurfaces in the form of conductivity gratings, which can bridge the momentum gap between incident radiation and surface plasmons. Here, we discuss singular graphene metasurfaces, whose conductivity is strongly suppressed at the grating valleys. By analytically characterising their plasmonic response via transformation optics, we first review the physical principles underlying these structures, which were recently found to exhibit broadband, tunable THz absorption. We characterise the spectrum with different common substrates and then move to study in further detail how conductivity gratings may be finely tuned by placing an array of charged gold nanowires at sub-micron distance from the graphene.

Keywords: Graphene / plasmonics / metasurfaces / terahertz / transformation optics / singularities / broadband

1 Introduction

Due to their low losses, high portability and ease of realisation compared to bulky components, metasurfaces are currently reshaping the field of metamaterials [1–5]. Interestingly, the optical properties of these structures may be widely tuned by engineering their sub-wavelength constituents. Transformation optics (TO) constitutes a powerful analytical tool to design metasurfaces, as it allows one to make intuitive predictions on how a given structure will guide electromagnetic fields, by exploiting the mathematical analogy between deformations of spatial coordinates and refraction [6–8]. A special class of coordinate transformations, called conformal maps, features the desirable property of leaving the Laplace equation unchanged between frames, so that they all share the same electrostatic potential. This fact makes them a valuable tool in the study of subwavelength plasmonic structures, which can be well described within the quasistatic limit [9]. This is most convenient in the case of structures with geometrical singularities, and it often enables analytic solutions, thus bypassing the need for expensive numerical computation [10,11].

Following this approach, theoretical advances have been made in the use of conformal TO for the design and characterisation of subwavelength plasmonic gratings, which bridge the momentum gap between free space radiation and surface plasmons [12–14]. Furthermore, the metasurface concept was hybridised with that of singular

structures in order to propose a new class of metasurfaces called 'singular metasurfaces' [15–17]. Similar to singular plasmonic nanoparticles [10,18], these structures are able to harvest radiation in their smooth regions, and adiabatically concentrate it near their sharp points. This results in a continuous set of resonance frequencies, in other words, the response of singular metasurfaces is broadband [15,16,19]. A particularly promising platform for the realisation of singular metasurfaces is graphene, thanks to its tunable conductivity.

Graphene is a promising plasmonic material, due to its high electron mobility, and the unrivalled field enhancement achieved by its THz plasmons [20–25]. However, coupling THz radiation to graphene surface plasmons (GSPs) requires the matching of the large momentum gap between them. One way of achieving this is by engineering a periodic pattern of the charge carrier concentration of graphene, and hence of its dynamical conductivity [12,26–28]. This can be realised by optical [29] or electrostatic [30] doping, or by patterning the graphene [31,32] or its environment [33,34]. Doping levels as high as $E_F \sim 2\,\mathrm{eV}$ (corresponding to carrier densities $n_s \sim 10^{15}\,\mathrm{cm}^{-2}$) have been reported [35,36]. Alternatively, the use of flexural waves to produce gratings for momentum-matching has been suggested [37,38].

In this work, we start by reviewing the concept and design of singular metasurfaces and their proposed implementation on free-standing graphene, thereby discussing a number of intuitive ways of understanding their behaviour. We then explore additional effects that would be present in three possible experimental configurations.

---

* Corresponding author: emanuele.galiffi12@imperial.ac.uk

We consider two different substrates placed in contact with the graphene, SiO$_2$ and hexagonal boron nitride (hBN), which can be patterned to form a grating (SiO$_2$) or flat (hBN). Finally, we consider how an array of charged gold nanowires close to homogeneously doped graphene induce a carrier density modulation on the graphene, which is used in further full-wave simulations of the THz response of the metasurface. Realistic experimental parameters are used throughout the paper.

2 Singular grating design

The conformal invariance of the Laplace operator ensures that different geometrical structures which can be mapped to each other via a conformal transformation share the same electrostatic potential, thus being spectrally equivalent in the quasistatic approximation, a feature of subwavelength plasmonic structures that has been referred to as 'hidden symmetry' [10,11,39–41]. However, the excitation of these shared eigenmodes depends strongly on the source used for each individual structure. For example, surface plasmons in homogeneously doped graphene may be excited from the near field, but would remain dark under plane wave illumination. By contrast, a conductivity grating can enable the far field-excitation of plasmons even at normal incidence [12,26,27,42].

In order to conformally design a grating, we start from a translationally invariant slab of thickness δ_0, positioned at $x = x_0$ as shown in the 'slab' frame $\tilde{z} = x + iy$ (Fig. 1a). Applying an exponential map $\tilde{z}_1 = e^{\frac{2\pi\tilde{z}}{d}}$ wraps each length d of this slab to a concentric annulus of radius e^{x_0} and thickness $e^{x_0}(e^{\frac{\delta_0}{d}} - 1)$ (Fig. 1b). We now invert the structure in Figure 1b with respect to the point iw_0, which lies inside the annulus, via the map $\tilde{z}_2 = \frac{1}{\tilde{z}_1 - iw_0}$ thus breaking rotational symmetry and realising a non-concentric annulus (Fig. 1c). Finally, shifting the origin to the axis of the smaller cylinder $\tilde{z}_2 = -iy_0$ in Figure 1c, and applying a logarithmic map $\tilde{z}' = x'(x,y) + iy'(x,y) = \frac{d'}{2\pi}\log\left(\tilde{z}_2(x_2,y_2) + iy_0\right)$ realises the desired modulated thickness $\delta(y')$ (Fig. 1d). The scale factor $\frac{d'}{2\pi}$ fixes the period d' of the grating [12]. The cascaded transformation thus reads:

$$\tilde{z}' = \frac{d'}{2\pi}\log\left(\frac{1}{e^{2\pi z/d} - iw_0} + iy_0\right) \tag{1}$$

and it can be shown that $y_0 = \frac{w_0}{e^{4\pi(x_0+d)/d} - w_0^2}$. In the following, we assume plane wave illumination at normal incidence. In order to incorporate this into our calculation, we invert the conformal transformation above to map plane waves in the grating frame to waves with periodically modulated phase front in the slab frame, where boundary conditions are applied.

We call a grating 'singular' if its valley point-thickness vanishes, i.e. if the black and red lines in Figure 1d touch. A moment of thought will reveal to the reader that, given that a conformal map preserves local
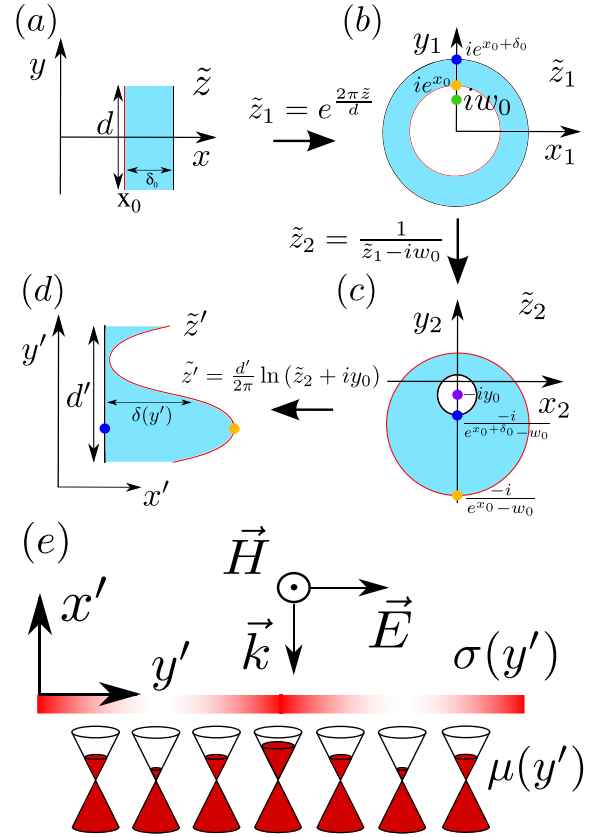

Fig. 1. Individual steps (a)–(d) of the conformal map used to generate a grating from a translationally invariant slab. The thickness of a metallic grating is equivalent to the conductivity profile of a inhomogeneously doped graphene sheet (e). The setup consists of a p-polarised wave, normally incident on a graphene sheet, whose chemical potential μ, and hence its conductivity σ is periodically modulated.

angles, no such map should ever be able to cause the two parallel lines in frame $\tilde{z}$ to cross on the same Riemann sheet. Nevertheless, this can be approached via the following limiting procedure: it is easy to see that, if the inversion point iw_0 (green dot) in Figure 1b tends to the point ie^{x_0} (orange dot) on the inner (red) circumference, the subsequent inversion will map the latter to $-i\infty$ in Figure 1c, resulting in the apex of the grating in Figure 1d to diverge. However, this divergence may be renormalised by simultaneously letting the periodicity $d \to \infty$ in Figure 1a, as doing so will rescale the entire geometry by a factor $\simeq \frac{2\pi}{d}$ [16]. Since the valley point-thickness of the grating is not affected by the aforementioned divergence, it will automatically tend to zero as a result of the rescaling [15,16].

Metallic singular structures, both localised [10,11,18] and as metasurfaces [17], have been proposed in the past. However, the tunability of graphene offers the opportunity of continuously approaching the singular limit within the same sample. This is typically realised by periodically modulating its charge carrier density via electrostatic gating, thus realising a conductivity grating [12–14]. Furthermore, the extremely subwavelength character of

graphene plasmons results in this system being accurately described by a quasistatic approximation, which is a natural playground for conformal TO.

The framework described above can be straightforwardly applied to graphene through the following consideration: the permittivity

$$\varepsilon(\omega) = 1 + \frac{i\sigma_g(\omega)}{\varepsilon_0 \omega \delta} \qquad (2)$$

of a thin metallic slab of conductivity $\sigma_g(\omega)$ and thickness δ is conserved across the conformal map [12]. Hence, by writing ε in the slab and in the grating frames, the modulated thickness $\delta(y')$ in the grating frame is straightforwardly shown to be proportional to a modulated conductivity profile according to $\sigma(\omega, y') = \frac{\delta(y')}{\delta_0}\sigma_g(\omega)$. In the limit $\delta_0 \to 0$, the modulation profile $\frac{\delta(y')}{\delta_0}$ becomes independent of δ_0. Thus, the transformation can be used to model a periodically doped graphene sheet, as illustrated in Figure 1e.

3 Results

3.1 Free-standing modulated graphene

As a first demonstration of the capabilities of these metasurfaces, we consider three gratings, increasingly close to the singular limit, surrounded by free space. Their conductivity modulation profiles, generated from a slab of (dimensionless) thickness $\delta_0 = 2 \times 10^{-3}$ and periods $d_1 = 2\pi$, $d_2 = 2.6 \times 2\pi$ and $d_3 = 5.3 \times 2\pi$ via the transformation described above, with modulation depths $w_0 = 0.55$, 0.8 and 0.9, respectively, are shown in log scale in Figure 2 (top inset). The apex-doping level is maintained fixed at a chemical potential $\mu \approx 1.5$ eV, while its valley point doping is gradually reduced, thus tending to a 'singular' point, where the conductivity σ_g, which is approximately proportional to the chemical potential μ in the Drude limit, is strongly suppressed. The periodicity $d' \approx 2.5\,\mu$m, temperature $T = 300$ K and a conservative electron mobility of $5000\,\text{cm}^2/(\text{V s})$ is assumed, which correspond to commonly achieved values in state-of-the-art experiments [31]. More details on the local random phase-approximated (RPA) conductivity model are in Appendix A and the analytical solution of the scattering problem may be found in [12,13,16]. The effect of approaching the singularity on the transmission spectra, shown in Figure 2, is twofold: on the one hand, the evident reduction in relative spacing between transmission dips shows the progressive merging of GSP resonances towards a continuum of modes (Fig. 2a). On the other hand, higher order GSPs, exhibiting stronger confinement and higher field enhancements (Fig. 2b), can now be excited with high efficiency from the far field.

In the non-singular regime (top), the metasurface is able to strongly excite surface plasmons at a discrete set of frequencies, which appear as transmission dips in Figure 2. By reducing the valley-point conductivity, more peaks are excited (middle), while their mutual spacing decreases. Further approaching the singular limit, several more modes
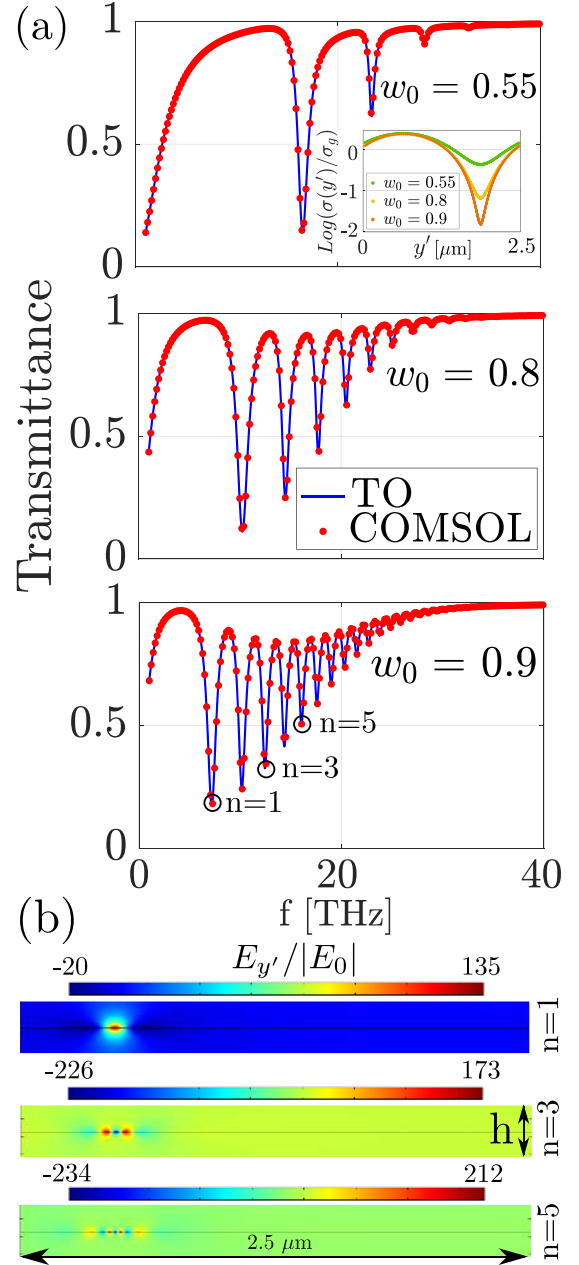

Fig. 2. (a) Transmission spectra for three metasurfaces increasingly close to the singular limit. COMSOL simulations (red dots) and analytic calculations performed with TO (blue lines) show perfect agreement. The top inset shows the spatial conductivity profile $\delta(y')/\delta_0 = \sigma(y')/\sigma_g$ along the metasurface. (b) In-plane component of the electric field normalized to the incident amplitude for the $n = 1$, 3 and 5 modes at $f \approx 7.4$, 12.4 and 15.9 THz, respectively. The vertical extent of all plots $h = 200$ nm, highlighting the increase in GSP confinement with mode order.

are strongly excited, and their resonant frequencies begin to merge in the far infrared (bottom). In this limit, the fields experience an extreme confinement near the singular point, thus challenging numerical approaches. Once the spacing between resonances becomes comparable to their
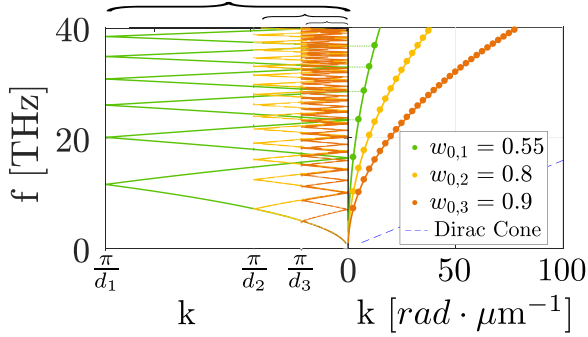
Fig. 3. The RHS shows the dispersion relations at normal incidence, constructed by assigning a wavevector $k_n = \frac{2\pi}{a}n$ to each resonance peak. The resonances are denoted by dots, while the horizontal lines are a guide to the eye. As shown in the LHS, the modes for the increasingly singular gratings can be equivalently found by folding the dispersion relation over a gradually narrower Brillouin zone, whose width is dictated by the effective periodicity d of the mother structure in the slab frame. The slab frame periods used are $d_1 = 2\pi$, $d_2 \approx 2.6 \times 2\pi$ and $d_3 \approx 5.3 \times 2\pi$.

broadening, the wealth of discrete surface plasmon resonances fully merge into a continuum of modes, which are strongly coupled to external radiation over a broad frequency band. In this limit, these atom-thick metasurfaces would act as broadband single-sheet absorbers, efficiently harvesting THz radiation over fractional bandwidths of nearly 200% [16].

Figure 2b shows the field profile of different GSP modes. Radiation is trapped in the smooth parts of the grating and is compressed as it travels towards the singularity, as is evident from the wavelength compression near the singular point shown in the field plot. It should be noted, however, that the scale of the GSP wavelength $\lambda_{\text{GSP}} \propto f^{-2}$ near the singularity quickly approaches the maximum lateral confinement of surface plasmons given by nonlocality, $\lambda_D \sim \lambda_0/300 \propto f^{-1}$ [34]. This sensitivity of the far field spectrum to nonlocality could be used to probe quantum nonlocal effects in graphene [43].

The broadband behaviour of singular gratings can be intuitively explained via our TO approach. In the quasistatic approximation, the slab and the grating frame share the same GSP spectrum, which is given by the quasistatic dispersion relation for GSPs [12]:

$$\varepsilon_1 + \varepsilon_2 + 4\pi i \sigma_g(\omega) \frac{|k|}{\omega} = 0 \qquad (3)$$

with ε_1 and ε_2 being the relative permittivities of the substrate and superstrate, $\sigma_g(\omega)$ the surface conductivity, k the in-plane wavevector and ω the angular frequency. However, in the grating frame the waves are quantised over a finite period d'. As described above, the singular limit may be conformally realised only by letting the length of the quantisation box of the plasmons in the slab frame $d \to \infty$. The consequence can be easily visualised by looking at the band structures in Figure 3 and considering that, as the quantisation box $d \to \infty$, the size of the first Brillouin

zone in the slab frame shrinks to zero, so that the modes at $k = 0$ become increasingly close to one another. The matching between the crossing of our folded dispersion relations with the frequency axis ($k = 0$) in Figure 3 (left) and the extended dispersion relation obtained from our calculations for each increasingly singular metasurface (right) confirms the above analysis. Hence, a singular metasurface, as opposed to a conventional one, exhibits a continuous spectrum.

Interestingly, this phenomenon can be related to what is known in high-dimensional field theories as compactification [15,44]. In fact, despite appearing to be a two-dimensional object, a singular grating contains, hidden in the singularity, a third dimension. Once again, the origin of this effect becomes apparent if we consider the equivalent structure in the slab frame. As the periodicity d of the system in the slab frame tends to infinity, an extra dimension is effectively generated along the y axis. The system is periodic along y, hence infinite, but the length d of each of these periods becomes itself infinite, in the singular limit. Hence, an additional dimension is being intruded along the y axis, so that, including the out-of-plane axis, the total number of dimensions present amounts to three. This additional dimension, hidden within the singularity in the grating frame, introduces a third spatial degree of freedom, which is freely available for the incoming radiation to satisfy the dispersion relation over a continuum of frequencies.

The ability of singular metasurfaces to merge the plasmonic dispersion relation enables the excitation of a much higher number of modes compared to a conventional subwavelength grating, since the resonances are shifted to a lower frequency region, where the conductivity of graphene $\sigma_g(\omega) \sim \frac{1}{\omega}$ suffices to efficiently capture the incoming THz waves. In fact, higher order GSP modes can now be efficiently excited and exhibit a much stronger confinement compared to their low order counterparts. This enables broadband harvesting of THz radiation [16].

3.2 Modulated graphene with SiO$_2$ grating

A possible way of modulating the conductivity of graphene is by applying a gate potential through a periodically patterned dielectric substrate (or superstrate). This would induce a periodic modulation of the carrier density in graphene with the same periodicity as that of the dielectric relief. This motivates us to consider a SiO$_2$ superstrate with modulated thickness placed on top of the graphene metasurfaces considered previously (top inset of Fig. 4). SiO$_2$ is a common material of choice for graphene-based heterostructures, and it features three surface optical phonon (SOP) bands in the THz [42], as described in Appendix B. Here, we study how the SOP bands affect the broadband spectra of the singular graphene metasurfaces. For illustration purposes, we consider only the THz scattering problem, assuming the local conductivity of the graphene to be proportional to the SiO$_2$ thickness.

The apex thickness of all SiO$_2$ gratings considered is 300 nm, whereas their valley-point thickness is gradually reduced, simultaneously with the minimum conductivity
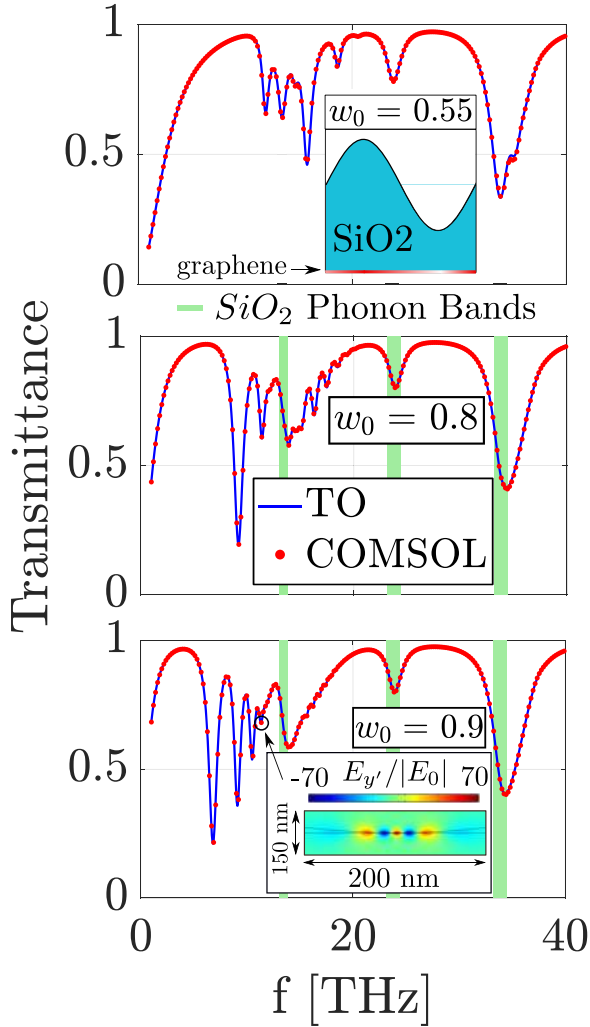
Fig. 4. The transmittance plots show the excitation of GSPs and SOPs for the three increasingly singular graphene metasurfaces covered by a similarly modulated SiO$_2$ superstrate. The presence of peaks due to SOPs in SiO$_2$ could pose an experimental challenge to a clear measurement of the close-to-singular plasmonic spectrum. The maximum thickness of the SiO$_2$ grating is 300 nm, whereas the minima are 50, 8 and 3 nm respectively (top to bottom). The bottom inset shows the 4th order GSP mode at $f \approx 11.3$ THz, showing a maximum (in-plane) field enhancement of ≈ 70, and a minimum vertical decay length of ≈ 9 nm. The maximum total field enhancement $|E|/|E_0| \approx 80$.

of the graphene, from 50 to 8, and finally to 3 nm, for $w_0 = 0.55$, 0.8 and 0.9, respectively. Their modulation is generated via the same transformation above, by placing the additional boundary at a (dimensionless) distance 0.3 from the graphene in the slab frame. The graphene modulations are analogous to the previous case. We solve this problem analytically, following the TO scheme used in [12], which only had to be generalised to account for the arbitrary period d of the structure in the slab frame. We benchmark our results with numerical full-wave simulations, demonstrating nearly perfect agreement, as shown in Figure 4.

Compared to the suspended graphene case, here the spectrum exhibits large additional features due to the excitation of SOPs, and their interaction with the GSP modes. As the singularity is gradually approached, more and more peaks move towards the low frequency region of the spectrum, and a wealth of GSP modes is concentrated within a narrow frequency band near $f \approx 15$ THz. However, the field enhancement achieved by these high order modes is at least an order of magnitude lower than in the case of free-standing graphene, due to the interaction with the SOP band. This is also reflected in the weaker contrast of the dips in the transmission spectrum. The latter might pose an additional challenge to the clear observation of this effect in graphene-SiO$_2$ heterostructures.

3.3 Modulated graphene with hBN substrate

The material that has so far demonstrated to be most promising for high-quality graphene heterostructures is hBN, primarily due to its matching of the crystalline structure of graphene, which improves the quality of graphene growth, and its intrinsically low losses [34,45,46]. However, hBN features two surface phonon bands: one affecting the out-of-plane component $\varepsilon_{||}$ of the permittivity tensor at 23–14 THz and one affecting its in-plane components $\varepsilon_{\perp}$ at 41–48 THz, as described in Appendix B. Hence, in order to anticipate the effect of these phonon modes on our GSP spectra, we consider substrates of thickness $h_{\mathrm{hBN}} = 20$ nm and 200 nm placed below the graphene conductivity gratings considered in Section 3.1, as shown in the top inset of Figure 5.

The transmission spectra resemble more closely the ones of free-standing graphene, compared to the case with SiO$_2$, thus demonstrating a very weak interaction of the incident radiation with the out-of-plane phonon band at ≈ 24 THz. This is due to the in-plane polarisation of the incident field, which does not directly interact with the out of plane component of the permittivity $\varepsilon_{||}$. On the other hand, the spectra show a reduction in transmission due to the in-plane phonon band at ≈ 41 THz, which is clearly more pronounced for thicker hBN substrates. However, this does not affect the observation of our GSP modes, since they are excited at much lower frequencies.

Finally, we highlight how the merging of the GSP modes is significantly more pronounced compared to the free-standing graphene case. This can be intuitively understood from the dispersion relation (Eq. (3)) which shows, assuming a Drude-like conductivity regime $\sigma_g \sim \frac{1}{\omega}$, that the GSP frequency $\omega \sim (\varepsilon_1 + \varepsilon_2)^{-1/2}$ scales approximately as the inverse square root of the sum of the permittivities of the dielectrics surrounding the graphene. As a consequence, very high field enhancements can be exploited by efficiently exciting higher order modes, whose resonant frequencies are now conveniently reduced, as shown in the bottom inset of Figure 5. On the other hand, it should be noted that the presence of the substrate will reduce the GSP wavelength, so that nonlocal effects will become appreciable at lower frequencies compared to the free-standing graphene case.
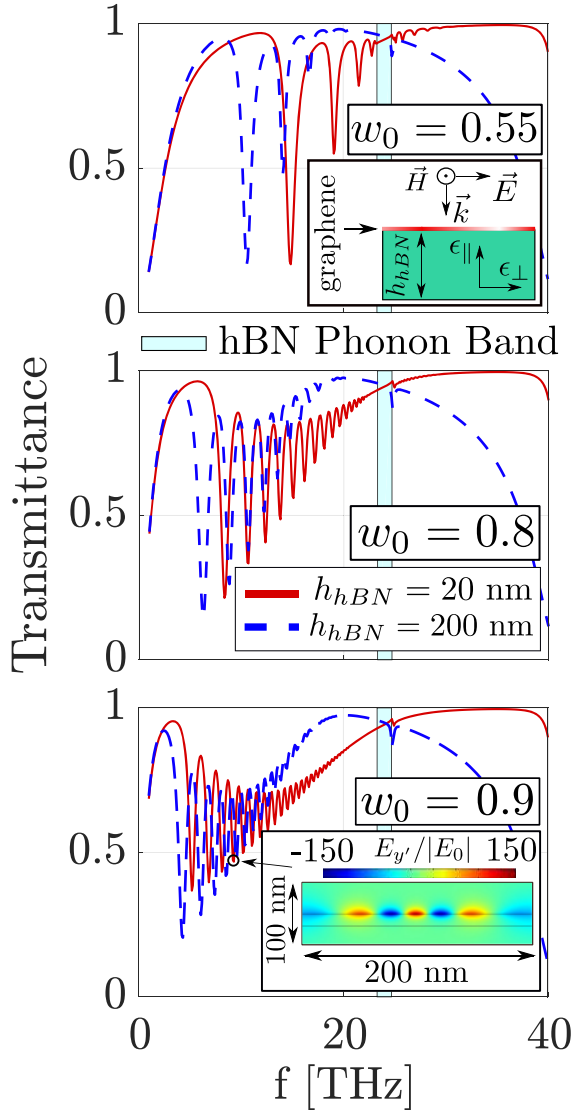
Fig. 5. Due to its horizontal polarisation, the incoming radiation can only weakly interact with the phonon band affecting the normal component of ε at ≈ 24 THz, so that the GSP spectrum is left intact by the presence of the hBN substrate even for significant thicknesses. In contrast, the in-plane phonon band is responsible for the strong transmittance dip at ≈ 41 THz. For our singular gratings, this lies way above the GSP frequency region. The field plot (bottom) shows the 4th order GSP mode for $h_{\mathrm{hBN}} = 20$ nm at $f \approx 9.3$ THz, exhibiting a maximum (in-plane) field enhancement $E_{y'}/|E_0| \approx 150$, and a minimum vertical decay length is ≈ 5 nm. The maximum total field enhancement $E|/|E_0| \approx 210$.

3.4 Electrostatically doped graphene via wire-array

In the final setup considered we show how the singular graphene conductivity grating can be generated by electrostatic doping with an array of metal wires. We consider a periodic array (period $d' \approx 2.5\,\mu$m along the x-axis) of charged (potential difference V) gold nanowires of radius $R = 80$ nm, vertically (y-axis) separated from free-standing, homogeneously biased graphene, by a gap
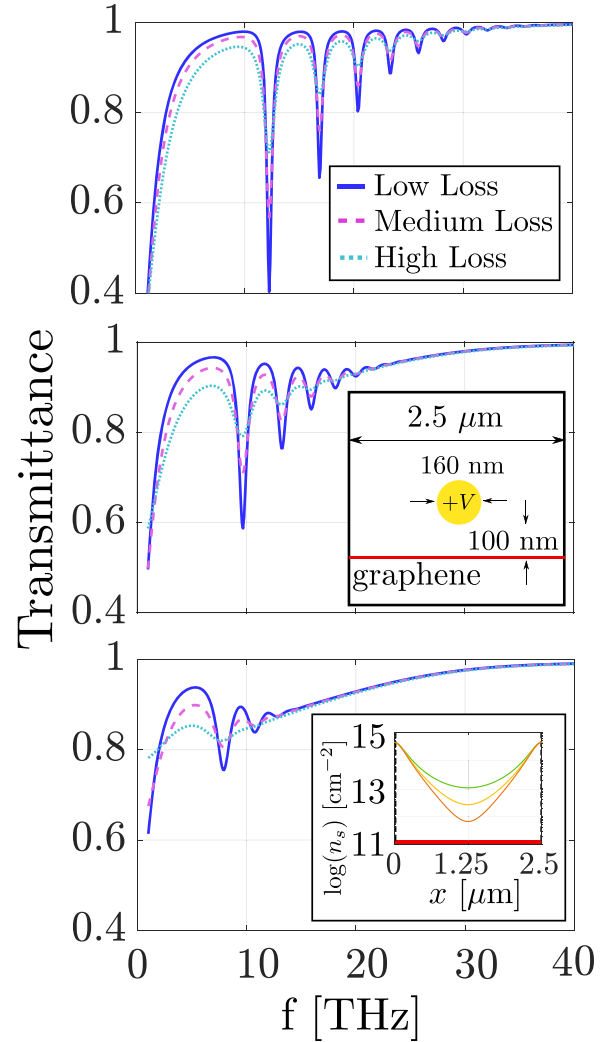

Fig. 6. The singular limit is approached by simultaneously increasing the voltage ($V = 1.03$, 1.23 and 1.33 eV from top to bottom) between a graphene sheet and an array of 160 nm-thick gold wires, and down-shifting the chemical potential of the whole sheet by a constant value (-0.11, -0.24 and -0.30 V from top to bottom). The increasingly high (blue to cyan lines) losses, corresponding to electron mobilities 2×10^4, 1×10^4 and 5×10^3 cm^2/(V s) result in a faster merging of the spectrum due to smearing of the transmittance dips. The dielectric function of gold is obtained from experimental data [47].

$a = 100$ nm, as shown in the mid-inset of Figure 6. By analytically computing the electrostatic potential of the wire array (Appendix C), we obtain the periodic charge carrier density pattern induced on the graphene:

$$n_s = \frac{2\varepsilon_0 V}{e \log\!\left(\dfrac{2a - R}{R}\right)} \sum_n \frac{a}{(x - nd')^2 + a^2} \qquad (4)$$

By tuning the wire voltage V and simultaneously adjusting the Fermi level of graphene via a constant bias (as could be realised e.g. via a flat back-gating), the singularity of the metasurface may be approached without

requiring multiple fabrications to tune the modulation levels. The possibility of dynamically tuning the spectrum is desirable for applications and would be helpful in an experiment as it would avoid intrinsic discrepancies between different samples. The resulting carrier densities are plotted in the bottom inset of Figure 6 in logarithmic scale. The carrier density at the apex is $\sim 4 \times 10^{14}\,\mathrm{cm}^{-2}$, while the valley-point values range from $\sim 10^{13}\mathrm{cm}^{-2}$, $\sim 1.5 \times 10^{12}\,\mathrm{cm}^{-2}$ to $\sim 6 \times 10^{11}\,\mathrm{cm}^{-2}$, as the singular limit is approached. We note that these values are typical experimental values. With these carrier density profiles, we calculate the chemical potential profile $\mu(x) = \hbar v_F \sqrt{|n_s(x)|}$, to feed into the conductivity model (Appendix A).

Given the derived inhomogeneous chemical potential, together with the electron mobility m (which we assume to be fixed by the quality of the graphene sample), we obtain the normalised scattering frequency as $\Gamma(x) = \frac{\hbar v_F^2}{m\mu(x)^2}$, as well as spatially inhomogeneous finite temperature contributions. Note that this is in contrast to the previous calculations, where Γ was taken as a constant.

As shown in Figure 6, these more realistic experimental considerations play an important role in the resulting transmission spectra, as the losses are significantly enhanced when the mobility is rescaled by the position-dependent chemical potential, which is suppressed near the singularity. In fact, if this is not accounted for, the lifetime of GSPs is not preserved across the spectrum, which explains why the broadening of the peaks in Figures 2–5 does not scale linearly with frequency.

The results in Figure 6 show a trend similar to the previous scenarios. We observe a systematic reduction of the GSP frequencies, and their relative spacing as the singular limit is approached. In this case, as the singularity is approached, the plasmon resonances effectively merge into a continuum faster than in the previous cases due to the more prominent effect of resistive losses in graphene. In contrast, no additional extinction was caused by the losses in gold, due to the weak field penetration at THz frequencies. On the other hand, in a real experiment, the emergence of nonlocality is likely to oppose the merging of the peaks. This is expected due to the longer Thomas–Fermi wavelength of the electrons in the depleted region of our conductivity gratings, which becomes comparable to the plasmon wavelength [43].

4 Conclusions and perspectives

In this work, we reviewed how, by spatially modulating the conductivity of graphene in a singular grating pattern, THz radiation can be efficiently harvested and coupled to GSPs over a broad band with an atomically thin layer. We used TO to provide insight and further clarification to the broadband behaviour exhibited by these metasurfaces, and their link to the concept of compactification. We stress that the singularity dominates the behaviour of these gratings. In fact, these effects are very robust to changes in geometrical parameters as long as the smooth part of the grating

allows the plasmons to adiabatically travel towards the singularity without significant reflection.

We then gave further details on experimental opportunities for realising these structures by exploring the effects introduced by the environment on the transmission spectra. Our conclusions highlight the fact that hBN constitutes the ideal substrate for the observation of the GSP spectra in the singular limit, whereas the SOP bands of SiO_2 may significantly interfere with GSP measurements. Finally, we discussed how the necessary spatial inhomogeneity of the graphene conductivity profile may be engineered by placing an array of metallic nanowires at sub-micron distance from a uniformly doped graphene sample, thereby enabling dynamic tunability of the GSP spectrum. Given the realistic parameters used in our calculations, we thus conclude that, assuming that sufficiently high quality graphene is used, the possibility of observing the merging of GSPs in a close-to-singular graphene metasurface is promising.

Finally, it is important to note that these singular metasurfaces are able to compress the plasmon wavelength to very short scales, such that $\lambda_{\mathrm{GSP,min}}$ near the singular point approaches the wavelength of the Dirac carriers $\lambda_0/300$. In this regime, nonlocal contributions to the graphene conductivity become significant. Heuristically, nonlocality will tend to oppose the effect of the singularity by pushing the resonances apart. Microscopically, this is due to the smearing of the charge density along the metasurface, which will become more prominent once the grating valleys become significantly depleted. Hence, singular graphene metasurfaces may serve as an effective experimental window into the quantum nonlocal features of Dirac carriers in graphene.

Appendix A: Graphene conductivity model

The local RPA conductivity of graphene is considered [48], which depends on frequency ω, chemical potential μ, temperature T and carrier's mobility m. This can be expressed as a sum of intraband and interband contributions, $\sigma_g = \sigma_{\mathrm{intra}} + \sigma_{\mathrm{inter}}$, as follows [48]:

$$\sigma_{\mathrm{intra}} = \frac{2ie^2 t}{\hbar\pi[\Omega + i\Gamma]}\ln\left[2\cosh\left(\frac{1}{2t}\right)\right], \qquad (A.1)$$

$$\sigma_{\mathrm{inter}} = \frac{e^2}{4\hbar}\left[\frac{1}{2} + \frac{1}{\pi}\arctan\left(\frac{\Omega - 2}{2t}\right) - \frac{i}{2\pi}\ln\frac{(\Omega + 2)^2}{(\Omega - 2)^2 + (2t)^2}\right], \tag{A.2}$$

where $\Omega = \hbar\omega/\mu$ and $t = k_B T/\mu$ are frequency and temperature normalised to the chemical potential, respectively. The normalised damping term is $\Gamma = \hbar/(\mu\tau)$,

where $\tau = m\mu/v_F^2$ is the carriers' scattering time, m is the electron mobility and $v_F = 9.5 \times 10^7 \, \text{cm s}^{-1}$ is the Fermi velocity [16].

Appendix B: Dielectric properties of substrates

In the THz regime, the dielectric function of SiO_2:

$$\varepsilon_{SiO_2} = \varepsilon_\infty + \sum_{j=1}^{3} f_j \frac{\omega_{TO,j}^2}{\omega_{TO,j}^2 - \omega^2 - i\omega\Gamma_{TO,j}} \quad (B.1)$$

is characterised by three transverse optical phononic bands, with $\omega_{TO,1} = 13.45$ THz, $\omega_{TO,2} = 23.8$ THz and $\omega_{TO,3} = 33.9$ THz, weights $f_1 = 0.751$, $f_2 = 0.150$ and $f_3 = 0.601$, and widths $\Gamma_{TO,1} = 8.01$ THz, $\Gamma_{TO,2} = 1.27$ THz and $\Gamma_{TO,3} = 1.27$ THz. The bands, centred at their respective $\omega_{TO,j}$ over their widths $\Gamma_{TO,j}$, are plotted in Figure 4 [42].

The anisotropic response of hBN is characterised by two reststrahlen bands, one for each permittivity component, of the form:

$$\varepsilon_j = \varepsilon_\infty \left(1 - \frac{\omega_{LO,j}^2 - \omega_{TO,j}^2}{\omega^2 - i\omega\Gamma_j - \omega_{TO,j}^2} \right) \quad (B.2)$$

where $j = \perp, \parallel$ (note, symbols are defined with respect to the axis normal to the surface, as customary with hyperbolic materials) are the in-plane and out-of-plane components of the relative permittivity respectively, with $\omega_{TO,\perp} = 41.07$ THz, $\omega_{LO,\perp} = 48.27$ THz, $\varepsilon_{\infty,\perp} = 4.87$, $\Gamma_\perp = 0.15$ THz, and $\omega_{TO,\parallel} = 23.38$ THz, $\omega_{LO,\parallel} = 24.88$ THz, $\varepsilon_{\infty,\parallel} = 2.95$, $\Gamma_\parallel = 0.12$ THz [45].

Appendix C: Electrostatic screening theory

The setup is shown in the mid-inset of Figure 6. For a cylinder of radius R with surface charge density σ_c the electric field reads $E = \frac{\sigma_c}{\varepsilon_0} R/r$, with r being the radial coordinate from the axis of the cylinder. The effect of the conductive plane parallel to the cylinder is straightforwardly obtained via the method of images, so that the complete potential reads

$$\phi(x,y) = -\frac{\sigma_c}{2\varepsilon_0} R \log \left\{ \frac{(x-x_0)^2 + (y-a)^2}{(x-x_0)^2 + (y+a)^2} \right\} \quad (C.1)$$

and the voltage difference between the wire and the sheet can be expressed in terms of the surface charge density as $V = -\frac{\sigma_c}{\varepsilon_0} R\log(R/2a - R)$. If we now consider an infinite array of metal cylinders, each placed at position $x_n = nd'$, $y = a$, the total potential is then given by:

$$\phi(x,y) = -\frac{\sigma_c}{2\varepsilon_0} R \sum_{n=-\infty}^{+\infty} \log \left\{ \frac{(x-nd')^2 + (y-a)^2}{(x-nd')^2 + (y+a)^2} \right\} \quad (C.2)$$

So that the charge carrier density n_s along the graphene induced by the electrode is $n_s = \varepsilon_0 E/e$ is:

$$n_s = \frac{2\varepsilon_0 V}{e\log\left(\frac{2a-R}{R}\right)} \sum_{n=-\infty}^{+\infty} \frac{a}{(x-nd')^2 + a^2} \quad (C.3)$$

where we substituted the expression for σ_c in terms of the potential V at the cylinder. This series is bounded from above by the convergent over-harmonic series $\sum_n \frac{1}{n^2}$. The convergence speed depends on the ratio a/d', which is intuitive, as the contribution from neighbouring cylinders becomes comparable as this ratio increases.

In our calculations we consider cylinders of radius $R = 80$ nm centred at a height $a = 180$ nm above the graphene, tune the wire voltage V to 1.03, 1.23 and 1.33 V (top to bottom in Fig. 6), and calculate the corresponding chemical potential $\mu(x) = \hbar v_F \sqrt{n_s(x)}$ while assuming a subsequent uniform down-shift of the chemical potential of the graphene sample by -0.11, -0.24 and $-0.30 \, \text{eV}$, respectively, so as to maintain a constant apex of our conductivity grating in the three cases considered, while reducing the valley-point conductivity.

References

1. C.L. Holloway, E.F. Kuester, J.A. Gordon, J. O'Hara, J. Booth, D.R. Smith, An overview of the theory and applications of metasurfaces: the two-dimensional equivalents of metamaterials, IEEE Antennas Propag. Mag. **54**, 10 (2012)

2. A.V. Kildishev, A. Boltasseva, V.M. Shalaev, Planar photonics with metasurfaces, Science **339**, 1232009 (2013)

3. N. Yu, F. Capasso, Flat optics with designer metasurfaces, Nat. Mater. **13**, 139 (2014)

4. N. Meinzer, W.L. Barnes, I.R. Hooper, Plasmonic meta-atoms and metasurfaces, Nat. Photonics **8**, 889 (2014)

5. H.-T. Chen, A.J. Taylor, N. Yu, A review of metasurfaces: physics and applications, Rep. Prog. Phys. **79**, 076401 (2016)

6. A.J. Ward, J.B. Pendry, Refraction and geometry in Maxwell's equations, J. Mod. Opt. **43**, 773 (1996)

7. J.B. Pendry, D. Schurig, D.R. Smith, Controlling electromagnetic fields, Science **312**, 1780 (2006)

8. U. Leonhardt, Optical conformal mapping, Science **312**, 1777 (2006)

9. J.B. Pendry, A.I. Fernández-Domínguez, Y. Luo, R. Zhao, Capturing photons with transformation optics, Nat. Phys. **9**, 518 (2013)

10. A. Aubry, D.Y. Lei, S.A. Maier, J.B. Pendry, Broadband plasmonic device concentrating the energy at the nanoscale: the crescent-shaped cylinder, Phys. Rev. B: Condens. Matter Mater. Phys. **82**, 125430 (2010)

11. J.B. Pendry, A. Aubry, D.R. Smith, S.A. Maier, Transformation optics and subwavelength control of light, Science (N.Y.) **337**, 549 (2012)

12. P.A. Huidobro, M. Kraft, R. Kun, S.A. Maier, J.B. Pendry, Graphene, plasmons and transformation optics, J. Opt. **18**, 044024 (2016)

13. P.A. Huidobro, M. Kraft, S.A. Maier, J.B. Pendry, Graphene as a tunable anisotropic or isotropic plasmonic metasurface, ACS Nano **10**, 5499 (2016)

14. P.A. Huidobro, S.A. Maier, J.B. Pendry, Tunable plasmonic metasurface for perfect absorption, EPJ Appl. Metamat. **4**, 6 (2017)

15. J.B. Pendry, P.A. Huidobro, Y. Luo, E. Galiffi, Compacted dimensions and singular plasmonic surfaces, Science **358**, 915 (2017)

16. E. Galiffi, J.B. Pendry, P.A. Huidobro, Broadband tunable thz absorption with singular graphene metasurfaces, ACS Nano **12**, 1006 (2018)

17. F. Yang, P.A. Huidobro, J.B. Pendry, Transformation optics approach to singular metasurfaces, Phys. Rev. B **98**, 125409 (2018)

18. Y. Luo, J.B. Pendry, A. Aubry, Surface plasmons and singularities, Nano Lett. **10**, 4186 (2010)

19. J.B. Pendry, A. Aubry, D.R. Smith, S.A. Maier, Transformation optics and subwavelength control of light, Science (N.Y.) **337**, 549 (2012)

20. F.H.L. Koppens, D.E. Chang, F.J. García de Abajo, Graphene plasmonics: a platform for strong light-matter interaction, Nano Lett. **11**, 3370 (2011)

21. L. Ju, B. Geng, J. Horng, C. Girit, M. Martin, Z. Hao, H.A. Bechtel, X. Liang, A. Zettl, Y.R. Shen, F. Wang, Graphene plasmonics for tunable terahertz metamaterials, Nat. Nanotechnol. **6**, 630 (2011)

22. A.Yu. Nikitin, F. Guinea, F.J. García-Vidal, L. Martín-Moreno, Fields radiated by a nanoemitter in a graphene sheet, Phys. Rev. B: Condens. Matter Mater. Phys. **84**, 195446 (2011)

23. A.N. Grigorenko, M. Polini, K.S. Novoselov, Graphene plasmonics, Nat. Photonics **6**, 749 (2012)

24. F.J.G. de Abajo, Graphene plasmonics: challenges and opportunities, ACS Photonics **1**, 135 (2014)

25. T. Low, P. Avouris, Graphene plasmonics for terahertz to mid-infrared applications, ACS Nano **8**, 1086 (2014)

26. N.M.R. Peres, Y.V. Bludov, A. Ferreira, M.I. Vasilevskiy, Exact solution for squarewave grating covered with graphene: surface plasmon-polaritons in the terahertz range, J. Phys.: Condens. Matter **25**, 125303 (2013)

27. T.M. Slipchenko, M.L. Nesterov, L. Martin-Moreno, A.Yu. Nikitin, Analytical solution for the diffraction of an electromagnetic wave by a graphene grating, J. Opt. (Bristol, UK) **15**, 114008 (2013)

28. P.-Y. Chen, C. Argyropoulos, M. Farhat, J.S. Gomez-Diaz, Flatland plasmonics and nanophotonics based on graphene and beyond, Nanophotonics **6**, 1239 (2017)

29. M. Baudisch, A. Marini, J.D. Cox, T. Zhu, F. Silva, S. Teichmann, M. Massicotte, F. Koppens, L.S. Levitov, F.J.G. de Abajo et al., Ultrafast nonlinear optical response of Dirac fermions in graphene, Nat. Commun. **9**, 1018 (2018)

30. M. Bokdam, P.A. Khomyakov, G. Brocks, Z. Zhong, P.J. Kelly, Electrostatic doping of graphene through ultrathin hexagonal boron nitride films, Nano Lett. **11**, 4631 (2011)

31. Y. Fan, N.-H. Shen, T. Koschny, C.M. Soukoulis, Tunable terahertz meta-surface with graphene cut-wires, ACS Photonics **2**, 151 (2015)

32. A.Yu. Nikitin, F. Guinea, F.J. Garcia-Vidal, L. Martin-Moreno, Surface plasmon enhanced absorption and suppressed transmission in periodic arrays of graphene ribbons, Phys. Rev. B: Condens. Matter Mater. Phys. **85**, 081405(R) (2012)

33. A. Vakil, N. Engheta, Transformation optics using graphene, Science (N.Y.) **332**, 1291 (2011)

34. D.A. Iranzo, S. Nanot, E.J.C. Dias, I. Epstein, C. Peng, D.K. Efetov, M.B. Lundeberg, R. Parret, J. Osmond, J.-Y. Hong et al., Probing the ultimate plasmon confinement limits with a van der Waals heterostructure, Science **360**, 291 (2018)

35. C.-F. Chen, C.-H. Park, B.W. Boudouris, J. Horng, B. Geng, C. Girit, A. Zettl, M.F. Crommie, R.A. Segalman, S.G. Louie et al., Controlling inelastic light scattering quantum pathways in grapheme, Nature **471**, 617 (2011)

36. D.K. Efetov, P. Kim, Controlling electron-phonon interactions in graphene at ultrahigh carrier densities, Phys. Rev. Lett. **105**, 256805 (2010)

37. M. Farhat, S. Guenneau, H. Bağcı, Exciting graphene surface plasmon polaritons through light and sound interplay, Phys. Rev. Lett. **111**, 237404 (2013)

38. J. Schiefele, J. Pedrós, F. Sols, F. Calle, F. Guinea, Coupling light into graphene plasmons through surface acoustic waves, Phys. Rev. Lett. **111**, 237405 (2013)

39. P.A. Huidobro, Y.H. Chang, M. Kraft, J.B. Pendry, Hidden symmetries in plasmonic gratings, Phys. Rev. B: Condens. Matter Mater. Phys. **95**, 1 (2017)

40. M. Kraft, Y. Luo, S.A. Maier, J.B. Pendry, Designing plasmonic gratings with transformation optics, Phys. Rev. X **5**, 031029 (2015)

41. M. Kraft, J.B. Pendry, S.A. Maier, Y. Luo, Transformation optics and hidden symmetries, Phys. Rev. B: Condens. Matter Mater. Phys. **89**, 245125 (2014)

42. P.A.D. Gonçalves, N.M.R. Peres, An introduction to graphene plasmonics (World Scientific, Singapore, 2016)

43. M. Lundeberg, Y. Gao, R. Asgari, C. Tan, B. Van Duppen, M. Autore, P. Alonso-Gonzalez, A. Woessner, K. Watanabe, T. Taniguchi, R. Hillenbrand, J. Hone, M. Polini, F.H.L. Koppens, Tuning quantum non-local effects in graphene plasmonics, Science **2735**, 1 (2017)

44. O. Klein, Quantentheorie und fünfdimensionale relativitäts-theorie, Z. Phys. **37**, 895 (1926)

45. A. Kumar, T. Low, K.H. Fung, P. Avouris, N.X. Fang, Tunable light-matter interaction and the role of hyperbolicity in graphene-hBN system, Nano Lett. **15**, 3172 (2015)

46. A. Woessner, M.B. Lundeberg, Y. Gao, A. Principi, P. Alonso-González, M. Carrega, K. Watanabe, T. Taniguchi, G. Vignale, M. Polini et al., Highly confined low-loss plasmons in graphene–boron nitride heterostructures, Nat. Mater. **14**, 421 (2015)

47. H.-J. Hagemann, W. Gudat, C. Kunz, Optical constants from the far infrared to the x-ray region: Mg, Al, Cu, Ag, Au, Bi, C, and Al_2O_3, J. Opt. Soc. Am. **65**, 742 (1975)

48. B. Wunsch, T. Stauber, F. Sols, F. Guinea, Dynamical polarization of graphene at finite doping, New J. Phys. **8**, 318 (2006)